Solid State Sciences 11 (2009) 1098–1106

Contents lists available at ScienceDirect

Solid State Sciences

journal homepage: www.elsevier.com/locate/ssscie

Investigation of changes in crystal and electronic structures by hydrogen within $LaNi_5$ from first-principles

A.F. Al Alam [a], S.F. Matar [a,*], M. Nakhl [b], N. Ouaïni [c]

[a] Université de Bordeaux, CNRS, ICMCB, 87 avenue du Docteur, Albert Schweitzer, F-33608 Pessac Cedex, France
[b] Université Libanaise, Faculté des Sciences, Fanar, Lebanon
[c] Université Saint-Esprit de Kaslik (USEK), Faculté des Sciences et Génie Informatique, Jounieh, Lebanon

ARTICLE INFO

Article history:
Received 27 January 2009
Received in revised form
26 February 2009
Accepted 26 February 2009
Available online 10 March 2009

PACS:
07.55.Jg
71.20.-b
71.23

Keywords:
Haucke phase
Hydride
DFT
VASP
ASW
Magnetic order
Chemical bonding
Bulk modulus
Electronic specific-heat coefficient

ABSTRACT

Hydrogenation of $LaNi_5$ *P6/mmm*, up to saturation brings modifications of the crystal structure with two possible space groups for $LaNi_5H_7$, *i.e.* $P6_3mc$ and *P31c*, determined experimentally. The energetics from computations within DFT allows pointing to the former as the most favorable one within a doubled cell along the *c*-axis with respect to $LaNi_5$. Results also show a compensation of the volume expansion effects favorable to the onset of magnetization by the chemical bonding involving Ni–H bond leading to vanishing moments.

1. Introduction

Haucke phases [1], AB_5 (A = rare-earth and B = *d*- and *p*-block elements), are known to absorb hydrogen up to the approximate composition of 6 H atoms per formula unit at mild conditions of temperature and pressure ($\sim$298 K and $\sim 2 \times 10^5$ Pa). This enables their use in rechargeable metal hydride batteries [2]. The hydrogen storage capacity for $LaNi_5$ amounts to $\sim$1.38 wt.% which exceeds that of liquid hydrogen by $\sim$40%. Nevertheless its gravimetric capacity is still small with respect to that of archetype hydride for applications, MgH_2, which amounts to $\sim$7.6 wt.%. It is also important to mention the remarkable feature of the rapid kinetics of the $LaNi_5$–H_2 system [3]. The experiment reports the formation of two hydrogen solutions, namely primary α-$LaNi_5H_{0.5}$ and more filled β-$La_2Ni_{10}H_{12}$ ($Z = 1$) [4,5]. The α phase crystallizes in the same space group (SG) as the pure alloy system whereas the β phase is characterized in two different SGs, namely $P6_3mc$ and *P31c*. For the latter hydride phase, neither the experiment nor previous *ab initio* calculations were able to discard either SGs. On the other hand, $LaNi_5$ is reported to be paramagnetic by the experiment [6]. With respect to this specific point, previous *ab initio* calculations have been performed but the resulting ground state configuration was different to the one reported by the experiment. For instance, early calculations performed within the augmented plane wave method (APW) showed that $LaNi_5$ is a *"very weak ferromagnet"* with a total moment of $0.69\mu_B$ [7]. Recent calculations gave total moment values such as 1.25 and $1.15\mu_B$ with the self-consistent linear muffin-tin orbital (LMTO) within the atomic sphere approximation (ASA) and the full potential (FP) LMTO methods respectively [8]. The authors commented these results by considering that the discrepancy of the total moment with respect to the experiment may be due to a delicate problem of calculation of the total energy

* Corresponding author. Tel.: +33 540002690; fax: +33 540002761.
E-mail address: s.matar@u-bordeaux1.fr (S.F. Matar).

1293-2558/$ – see front matter © 2009 Elsevier Masson SAS. All rights reserved.
doi:10.1016/j.solidstatesciences.2009.02.026

when the material is in a transitional state between a ferromagnetic and a paramagnetic states.

In this paper the electronic structure, energetics and magnetic ground state configuration of $LaNi_5$ and its saturated hydrogen β solution are analyzed from first-principles. The calculations are done with two complementary methods built within the density functional theory (DFT) [9–11] : a pseudo-potential (PP) method and an all-electron method. Using the PP method, we first revisit the symmetry of the β models to check for the most stable SG from both a structural and an energetic points of view. We also study the binding of hydrogen within the host lattice. The latter property is further evaluated by computing an additional hypothetic intermediate hydride model $LaNi_5H_3$ at the SGs of both the pure alloy and the β hydride systems. Secondly we examine the ground state of $LaNi_5$ by evaluating the electronic band occupations in both non-spin polarized (NSP) and spin polarized (SP) configurations provided by all-electron method. Finally, we study the energetics of hydrogen uptake in the β hydride as far as it is generally controlled by a size factor and an electronic factor. The volume expansion brought by hydrogen insertion in the host lattice usually induces a magnetization in such systems anticipated namely at the *d*- and *p*-block elements constituents. In the case of $LaNi_5$ one can presume the onset of a local magnetic moment carried by nickel atoms. It is important to study the magnetization of the hydride system relevant to the interplay of magnetovolume effects *versus* the chemical bonding of hydrogen with the different atomic constituents, especially with nickel atoms.

2. Crystal structures

$LaNi_5$ system crystallizes in the hexagonal $CaCu_5$-type, *P6/mmm* SG, Haucke structure [1]. For this phase, depicted in Fig. 1(b) and (c), La atoms occupy Wyckoff general position 1a at (0, 0, 0), while Ni atoms lye in two nonequivalent crystallographic sites: 2c at (1/3, 2/3, 0) and 3 g at (1/2, 0, 1/2). When hydrogen is absorbed into the lattice, a primary solid solution (the α phase) is formed without any change in the general crystal symmetry [4]. For space group *P6/mmm* one can argue around five possible hydrogen sites namely octahedral 3f (*2La–2Ni*$_{2c}$*–2Ni*$_{3g}$) and tetrahedral 4h (*Ni*$_{2c}$*–3Ni*$_{3g}$), 6m (*2La–2Ni*$_{3g}$), 12o (*La–Ni*$_{2c}$*–2Ni*$_{3g}$) and 12n (*La–2Ni*$_{3g}$*–Ni*$_{3g}$). The 3f and/or 12n sites have been most frequently concluded as the favorable occupation sites [4,12–14]. One can explain this with respect to the atomic surroundings of hydrogen within the former octahedral site on one hand and the reported hole size of the latter tetrahedral site of ~0.408 Å on the other hand which is concomitant to the Westlake criterion [15] that imposes a minimum interstitial hole size of 0.40 Å. Consequently, the 6m site cannot be ruled out with its hole radius of ~0.551 Å [13]. However a saturated hydride (the β phase) exists with two possible ordered structures as reported by neutron diffraction data [5]. These have the *P6*$_3$*mc* and the *P31c* symmetries respectively. They both show a doubled unit cell along the *c*-axis. Within the SG *P31c*, La atoms are located in special 2a position at (0, 0, z). Ni atoms are found within three nonequivalent positions: Ni1 in six-fold 6c position at (x, y, z) and Ni2(3) in two-fold 2b position at (1/3, 2/3, z). There are fourteen hydrogen atoms at three different crystallographic sites, namely 6c (H1) with an octahedral surrounding (*2La–2Ni1–Ni2–Ni3*) and 2b (H2) and 6c (H3) with a tetrahedral surrounding (*3Ni1–Ni2* and *2La–2Ni1* respectively). For more details refer to Fig. 1(a). The difference between the two SGs is relevant to the presence of a mirror plane within *P6*$_3$*mc* for the site 6c which leads to a particular position (x, $\bar{x}$, z) with respect to (x, y, z) in *P31c*. Thus Ni and H atoms are found within the hydride with the *P6*$_3$*mc* symmetry in the same locations and with the same foldings except for Ni1 which occupies a position that only differs from its *P31c* homologue by a mirror symmetry shift along the y-ordinate direction. In the following, the hydride phases crystallizing with SGs *P6*$_3$*mc* and *P31c* will be referred to as β1 and β2 respectively. A sketch of the β1 structure is given in Fig. 1(a).

3. Theoretical framework of computations

Two computational methods were used in the framework of DFT. A PP approach within the Vienna *ab initio* simulation package

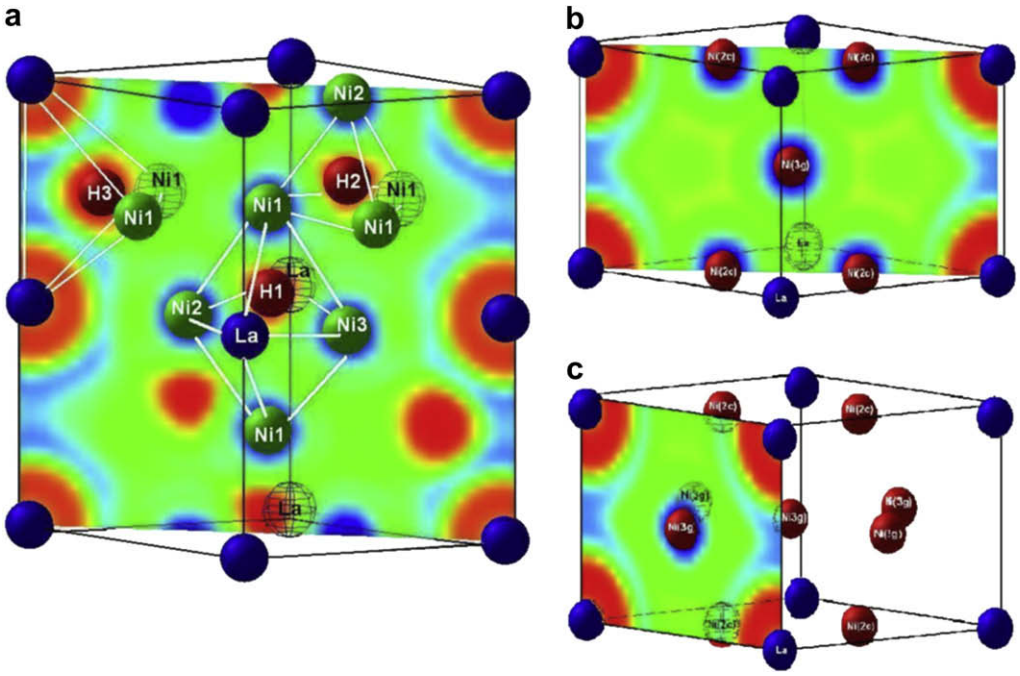

Fig. 1. (Color online) Crystal structure and electron localization functions maps for: $LaNi_5$ (b,c) and its β1 model for the saturated hydride system (a). Within the pure alloy, La atoms (blue spheres) are located at the cell corners and Ni atoms at the 3g site occupy the plane z = 1/2 which is perpendicular to the text plane. This leaves Ni atoms within 2c positions at the base planes.

(VASP) code [16] was firstly used to optimize the starting structures for the different hydride phases using projector augmented wave (PAW) [17,18] potentials built within the generalized gradient approximation (GGA) [20] scheme. The optimization of the structural parameters is performed until the forces on the atoms are less than 0.02 eV/Å and all stress components are below 0.003 eV/Å^3. The calculations were converged at an energy cut-off of 336.95 eV for the plane-wave basis set. The tetrahedron method with Blöchl corrections [17] as well as a Methfessel–Paxton scheme [21] for conducting systems were applied for both geometry relaxation and total energy calculations. Brillouin zone (BZ) integrals were approximated using the special Γ centered k-point grids adapted for hexagonal cells with a starting mesh of 4*4*4 up to 8*8*8 for best convergence and relaxation to zero strains. This sampling of the BZ is equivalent to that given by Monkhorst and Pack [22] with a shift of (1/2, 1/2, 1/2) from the origin of the latter and vice versa. Further, from PP calculations a mapping of the electrons within the lattice can be obtained. This provides an insight into the charge density distribution as well as into the localization of electrons around the chemical constituents which gives a view of the bonding in systems. The latter is the electron localization function (ELF) introduced by Becke and Edgecombe [23,24]. It allows determining the amount of localization of electrons with respect to the free electron gas distribution. The dimensionless ELF magnitude ranges from 0 to 1 with ELF = 1/2 corresponding to the free electron gas distribution. These three extreme situations will be illustrated by three sets of colors: ELF = 0 points to no localization (blue contours), ELF = 1 points to strong localization (red contours) and ELF = 1/2 with green contours.

All-electron calculations were performed using the scalar-relativistic implementation of the augmented spherical wave (ASW) method [25,26]. These computations are based on DFT and the GGA scheme as parameterized by Wu and Cohen [27]. In the ASW method, the wave function is expanded in atom-centered augmented spherical waves, which are Hankel functions and numerical solutions of Schrödinger's equation, respectively, outside and inside the so-called augmentation spheres. In the minimal ASW basis set, we chose the outermost shells to represent the valence states and the matrix elements were constructed using partial waves up to $l_{max}+1=4$ for La, $l_{max}+1=3$ for Ni and $l_{max}+1=2$ for H. It needs to be said that calculations are started for neutral atom configurations. They are *ab initio* and self-consistent with increasing k-points precision in the hexagonal BZ. Convergence is obtained when negligible variations for the charges ($\Delta Q = 10^{-8}$) and for the total energy ($\Delta E = 10^{-7}$ eV), are observed between two successive iterative cycles. In order to optimize the basis set, additional augmented spherical waves were placed at carefully selected interstitial sites (IS). The choice of these sites as well as the augmentation radii were automatically determined using the sphere-geometry optimization algorithm [28]. Self-consistency was achieved by a highly efficient algorithm for convergence acceleration [29]. The BZ integrations were performed using the linear tetrahedron method with up to 504 k-points within the irreducible wedge [17,26]. The efficiency of this method in treating magnetism and chemical bonding properties in transition-metal and rare-earth compounds has been well demonstrated in recent years [30–32]. The results obtained from DFT based calculations provide accurate indications to quantities such as the magnitudes of the magnetic moments, the nature and energy position of the states with respect to the Fermi level (E_F), the ground state configuration from relative energies etc. However a tool is needed to provide information about the nature of the chemical bond between two atomic constituents. This can be obtained from different available schemes, such as the crystal orbital overlap population (COOP) [33], the crystal orbital Hamiltonian population (COHP) [34] or the "covalent bond energy" (ECOV) [35] criteria. The latter combines both COHP and COOP so as to make the resulting quantity independent of the choice of the zero of potential. In the present work, the ECOV criterion was used for the chemical bonding analysis. In the plots, negative, positive and zero magnitudes of the unit less ECOV are indicative of bonding, antibonding, and nonbonding interactions respectively.

4. Pseudo-potential computations

4.1. Geometry optimization results

$LaNi_5$ [1] as well as its α and β hydride phases [5,13] are characterized by the experiment which established two possible SGs for the β phase, *i.e. P31c* and *P6$_3$mc*. It is then necessary to optimize the geometry of both systems prior to further calculations. From energy differences this should help pointing to the favorable symmetry for the saturated hydride as the one with the most stable energy between the two β models. It is worth mentioning that a similar attempt has been made before from first-principles computations without being able to discard either of the two SGs with respect to the total energy values of the optimized structures [36]. Nevertheless the internal parameters for both models were very close to those generated with SG *P6$_3$mc* whereby the authors concluded that the latter SG is more favorable. Also calculations performed by the same authors without geometry optimization were energetically favorable with respect to the SG *P6$_3$mc*. The pure alloy was also optimized to establish an equation of state which allows to compare quantities such as the equilibrium volume and bulk modulus with the hydride models. Primary α phase has the composition $LaNi_5H_{0.5}$ with several possible hydrogen insertion sites as discussed in section 2. A hydride model was optimized with a fully occupied 3f site resulting into a composition such as $LaNi_5H_3$ in order to avoid any breaking of the symmetry. This model can be considered as an intermediate hydride phase and compared to the pure alloy with respect to the pressure effects brought by the insertion of hydrogen in the host lattice. From the latter intermediate hydride a model was built with a doubled cell along the *c*-axis resulting into a composition such as $La_2Ni_{10}H_6$ ($Z=2$). An additional model with the same SG of the $\beta 1$ hydride model was also considered. Within this model H occupies the octahedral 6c sites resulting into an intermediate hydride $La_2Ni_{10}H_6$ ($Z=1$). This choice of H occupation site was done with respect to the other intermediate model which holds H in an octahedral site. As far as the difference between $\beta 1$ and $\beta 2$ models does not affect the surroundings of hydrogen atoms in their insertion sites (see section 2) there was no need to consider a model with the same SG of the $\beta 2$ hydride model. The latter two models are then important to establish a comparison with the saturated hydride system with respect to the binding of hydrogen within the host lattice. It is important to mention that the geometry optimizations are based on a spin degenerate configuration despite the paramagnetic character of $LaNi_5$. This is due to the fact that the spin directions are not linked to the crystalline structure (such as in noncollinear spin systems), *i.e.* the system is invariant under a general common rotation of all spins. While in the presence of spin orbit interaction SOI (collinear spin along the z direction) the spin directions become linked to the crystalline structure. Since in the case of $LaNi_5$ there is no SOI then assuming spin degeneracy is less significant with respect to the geometry optimization issues.

In a first step a geometry optimization was carried out on $LaNi_5$ using the PP based method (VASP). The starting internal parameters (see section 2) as well as the lattice constants ($a=5.017$ Å and $c=3.986$ Å) are taken from the experiment [1]. The resulting structure was found similar to the experimental one with respect to

the SG symmetry and the atomic species positions. The optimized lattice parameters values are such as ($a = 5.001$ Å) and ($c = 3.963$ Å) which are less than 1% lower than the experiment. This gives confidence to the optimization scheme and the used potentials. Now more complicated structures such as the hydride phases can be optimized.

The crystal structures of both β phase hydrides are described in section 2. The initial parameters for the special positions of the different atomic constituents are those given by the experiment [5]. A detailed description of the initial internal parameters for the starting optimization calculations is given in Table 1. An analysis of the optimized parameters can be then performed based on the listed informations. The value of the ratio c/a will be considered for the discussion of the optimized lattice constants with respect to the experiment. This ratio is 1.8 and 0.5% larger than its experimental values for the $\beta 1$ and $\beta 2$ models respectively. The internal parameters in both models are closer to the symmetry of SG $P6_3mc$ with respect to $P31c$. In previous *ab initio* calculations [36] showing the same trends, the authors pointed towards $P6_3mc$ as the favorable SG for the hydride system. Nevertheless this must be confirmed by a comparison of the total energies.

4.2. Energetics and equation of state

In order to obtain the equilibrium volumes and confront them with the experiment, (energy, volume) values were computed around the experimental data. The resulting $E(V)$ curves are plotted in Fig. 2(a) and (b) for $LaNi_5$, $\beta 1(2)$ hydride models and all the intermediate hydride models. The resulting equilibrium volumes for the saturated hydride models are 218.6 and 219.0 Å^3 for $\beta 1$ and $\beta 2$ respectively. These values are close to the experimental volume which amounts to 217.9 Å^3. The volume of $LaNi_5H_3$ model is larger than that of the pure alloy by ~ 12 Å^3. To compare the volume expansion brought by H insertion within the intermediate hydride with that of the saturated hydride models, one needs to consider both $La_2Ni_{10}H_6$ ($Z = 1$) and ($Z = 2$) models. Fig. 2(b) shows that these two intermediate models have very close $E(V)$ curves. This also results into very close equilibrium volumes of ~ 196 Å^3. Then the volume differences with the saturated hydride result to a β model volume larger by ~ 23 Å^3 with respect to $La_2Ni_{10}H_6$ models. This amount should be divided by two in order to compare it with the difference between between the pure alloy and $LaNi_5H_3$. This results into a value of ~ 11.5 Å^3 which is close to the volume difference between $LaNi_5$ and $LaNi_5H_3$. The cohesive energy of the hydride system E_{coh} is another significant quantity that can be investigated using the equilibrium energy values. E_{coh} describes the binding of hydrogen within the lattice and is expressed as follows:

$$E_{coh} = \frac{1}{n}[E(LaNi_5H_n) - E(LaNi_5)] - \frac{1}{2}E(H_2),$$

Here n is the amount of hydrogen present in the host lattice. $E(LaNi_5H_n)$, $E(LaNi_5)$ represent the total energies of the hydride models and the pure alloy system respectively. These are given in the inserts of Fig. 2(a) and (b). $E(H_2)$ is the energy of the dihydrogen molecule (−6.595 eV) which is computed by considering a cubic supercell of lattice parameter 4.5 Å. This value compares well with the literature value of −6.650 eV [37]. The obtained E_{coh} magnitudes are such as −0.099, −0.301 and −0.299 eV for $LaNi_5H_3$, $\beta 1$ and $\beta 2$ models respectively. The latter two values compare well with the heat of formation given by the literature which ranges from 0.332 to 0.363 eV/mol H_2 [38,39]. As for the intermediate phase it is clear that hydrogen is less bound to the host lattice. This is relevant to the fact that it is (i) a hypothetic model and (ii) an intermediate phase which explains the formation of a saturated hydride where H is more bound. Nevertheless E_{coh} values for the $La_2Ni_{10}H_6$ models are −0.218 and −0.195 eV for SGs $P6_3mc$ and $P6/mmm$ respectively. This provides an explanation for the cell doubling upon the uptake of more than one H per $LaNi_5$. This cell doubling ensures a more bound H in the host lattice and the more negative energy for SG $P6_3mc$ point to the contribution of the latter to the stability of the hydride phase. In the following the intermediate model with SG $P6_3mc$, *i.e.* $La_2Ni_{10}H_6$ ($Z = 1$), will be considered for comparison with both $LaNi_5$ and $\beta 1(2)$ models. On the other hand, calculations of the bulk modulus B_0 are possible through $E(V)$ curve fitting with a Birch 2nd order equation. The obtained magnitudes are $\sim$ 134.9, 129.8, 122.9 and 122.7 GPa for $LaNi_5$, $La_2Ni_{10}H_6$ ($Z = 1$), $\beta 1$ and $\beta 2$ models respectively. This is indicative of the larger compressibility of the hydride phase, with respect to $LaNi_5$, under hydrostatic pressure. The magnitude of B_0 decreases by $\sim$ 5 and 7 GPa while passing from pure alloy to the saturated hydride through the intermediate hydride phase. This is related to volume expansion seen earlier. Recent calculations performed for B_0 [40] resulted into a value of 126.4 GPa for $LaNi_5$ which is closer to the experiment (126.8 GPa) [41] than the value reported herein. In order to evaluate the β phase SG we considered the relative energy ΔE which is the difference between the equilibrium energies resulting from $E(V)$ curves of both $\beta 1$ and $\beta 2$ models. ΔE favors the $\beta 1$ model by 0.015 eV. This value is 1.5 times larger than the one given by previous calculations with a similar approach [36] which amounts to 10^{-2} eV in the favor of the $\beta 2$ model. Thus neither of the two SGs can be discarded by a PP approach which slightly favors the $\beta 1$ model in the present calculations.

Table 1
Internal parameters of the $\beta 1$ and $\beta 2$ models for the saturated hydride $La_2Ni_{10}H_{14}$ ($Z = 1$) from geometry optimization calculations using VASP code. Cell parameters a and c are given in Å.

$P6_3mc$ experiment				$P6_3mc$ optimized		
	a		c	a		c
	5.409		8.600	5.332		8.626
	x	y	z	x	y	z
La	0	0	0.022	0	0	0.022
Ni1	0.498	$\bar{x}$	0.250	0.499	$\bar{x}$	0.252
Ni2	1/3	2/3	0.002	1/3	2/3	0.006
Ni3	1/3	2/3	0.489	1/3	2/3	0.482
H1	0.504	$\bar{x}$	0.056	0.506	$\bar{x}$	0.059
H2	1/3	2/3	0.814	1/3	2/3	0.819
H3	0.160	$\bar{x}$	0.280	0.149	$\bar{x}$	0.275
$P31c$ experiment				$P31c$ optimized		
	a		c	a		c
	5.409		8.600	5.315		8.492
	x	y	z	x	y	z
La	0	0	0.004	0	0	0.025
Ni1	0.517	−0.486	0.250	0.500	0.502	0.258
Ni2	1/3	2/3	0.006	1/3	2/3	0.011
Ni3	1/3	2/3	0.497	1/3	2/3	0.488
H1	0.510	−0.490	0.057	0.506	0.494	0.066
H2	1/3	2/3	0.830	1/3	2/3	0.825
H3	0.154	−0.168	0.299	0.146	0.852	0.278

4.3. Analysis of the electron localization function (ELF)

Fig. 1 shows the electron localization function mapping for $LaNi_5$ (b,c) and the $\beta 1$ model (a). A diagonal plane along the c-axis cuts through H and La for Fig. 1(a) and La and Ni for Fig. 1(b). While Fig. 1(c) shows the ELF along the plane (0 0 0). For $LaNi_5$ it is clear from the yellow distorted pentagon shapes between lanthanum and nickel, *i.e.* in Fig. 1(b), that there is a charge transfer between

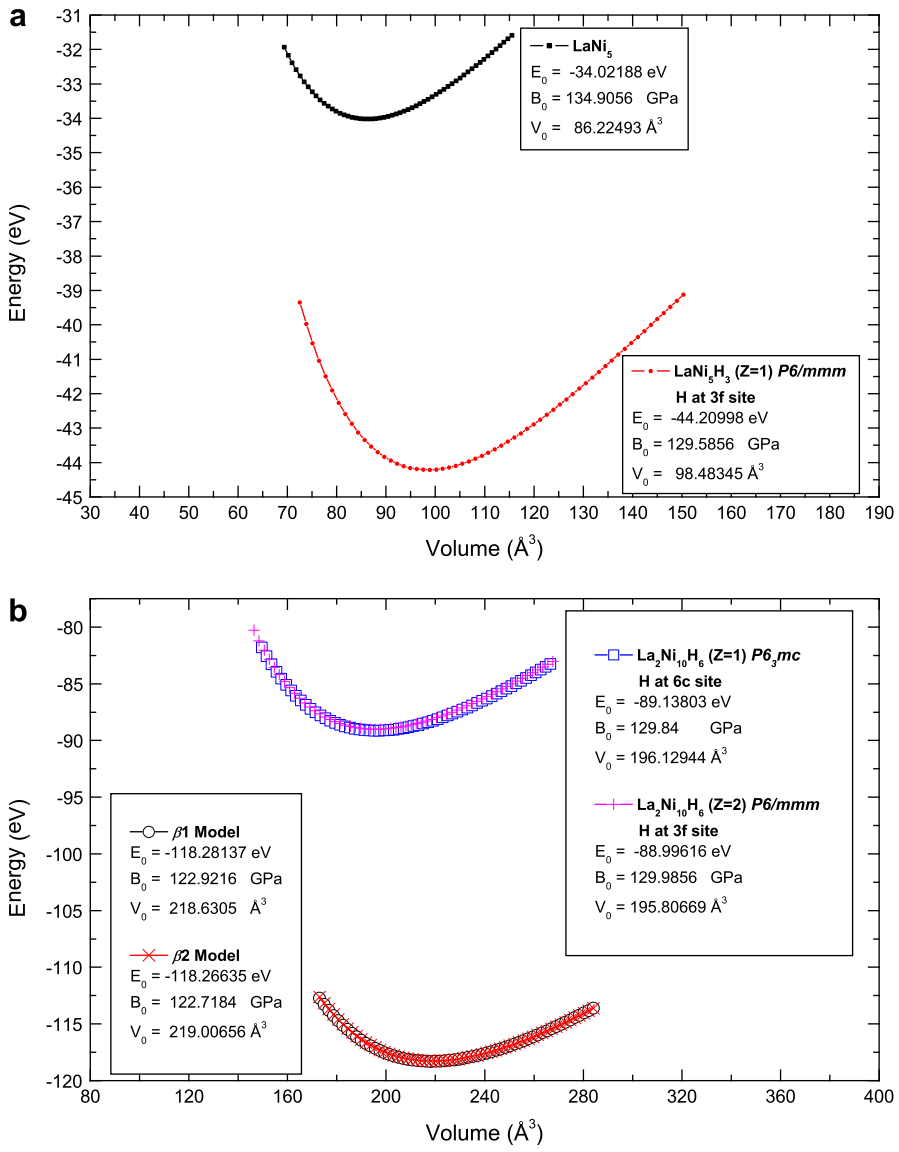

Fig. 2. (Color online) Energy as a function of cell volume curves for: $LaNi_5$, $LaNi_5H_3$ ($Z=1$) hydride model (a) and $\beta 1(2)$, $La_2Ni_{10}H_6$ hydride models (b).

the different atomic constituents. Further, one can notice the green areas between the atomic species (Fig. 1(b) and (c)). This points to a smeared electron distribution within the system similarly to a free electron like character expected within a metallic network. On the other hand, a strong localization is seen around hydrogen sites within the hydride system (see Fig. 1(a)). This agrees with the *"hydride"* picture of the system, *i.e.* with negatively charged hydrogen.

5. All-electron ASW computations

Since neither a neutron diffraction experimental characterization nor a PP theoretical computation were decisive to give a conclusion about the real SG for the β phase hydride system another step can be considered. This can be done by inserting the optimized data in an all-electron scheme such as the one used in the ASW method and perform the calculations within. Then the calculated energy differences might point toward the favorable SG. The crystal parameters provided by the VASP geometry optimizations (Table 1) were used for the input of all-electron calculations. The computational procedure follows a protocol through which a non-magnetic (NM) configuration is firstly assumed, meaning that spin degeneracy is imposed for all valence states with equal spin occupations. This configuration should not be confused with a paramagnet since $LaNi_5$ is known to have a paramagnetic ground state. Such NM computations are relevant at two levels (i) to carry out an analysis of the partial atom projected densities of states (PDOS) at the Fermi level within a mean field theory with respect to a possible magnetic instability in such a configuration and (ii) to analyze the chemical bonding between the different atomic constituents. Subsequent spin polarized (SP) calculations with different initial spin populations, *i.e.* majority $\uparrow$ -spin and minority $\downarrow$ -spin populations, can lead at self-consistency either to finite or zero local moments within an implicit long-range ferromagnetic order.

From the calculations, the energy difference which follows the expression $\Delta E = E_{\beta 1} - E_{\beta 2}$ shows that the $\beta 1$ model is $\sim$ 1.65 eV more stable. This difference points to $P6_3mc$ as the most probable space group for the β phase hydride. It is important to mention that first-principles calculations derived from a tight-binding linear

muffin-tin orbital method (TB-LMTO) without optimizing the structure comforted this last hypothesis [44].

Further, other sets of computations were performed for hydrogen–free models, at the same volume of the $\beta 1$ model. This simulates the manner in which the volume expansion (negative pressure) affects the magnetic behavior of the different atomic species. These effects can be important in such intermetallic systems as far as the onset of the magnetic moment is due to interband spin polarization, *i.e.* it is mediated by the electron gas in a collective electrons approach contrary to oxide systems where the magnetization is of intraband character, and hence, is less affected by volume changes such as those induced by pressure [42].

5.1. Spin degenerate calculations

5.1.1. Density of states

The PDOS of all the atoms from all the constituents present in the lattice, for $LaNi_5$ and the $\beta 1$ model are sketched in Fig. 3(a) and 3(b) respectively. Energies are referred to the Fermi level E_F. Looking firstly at the general shape of the PDOS for pure alloy system one can observe that the Fermi level is situated at the peaks of both Ni with a predominance in terms of intensity for the states of nickel atoms at 3g positions. This can be relevant to the fact that Ni at 2c and 3g sites are found with the occupation ratio 2:3 respectively.

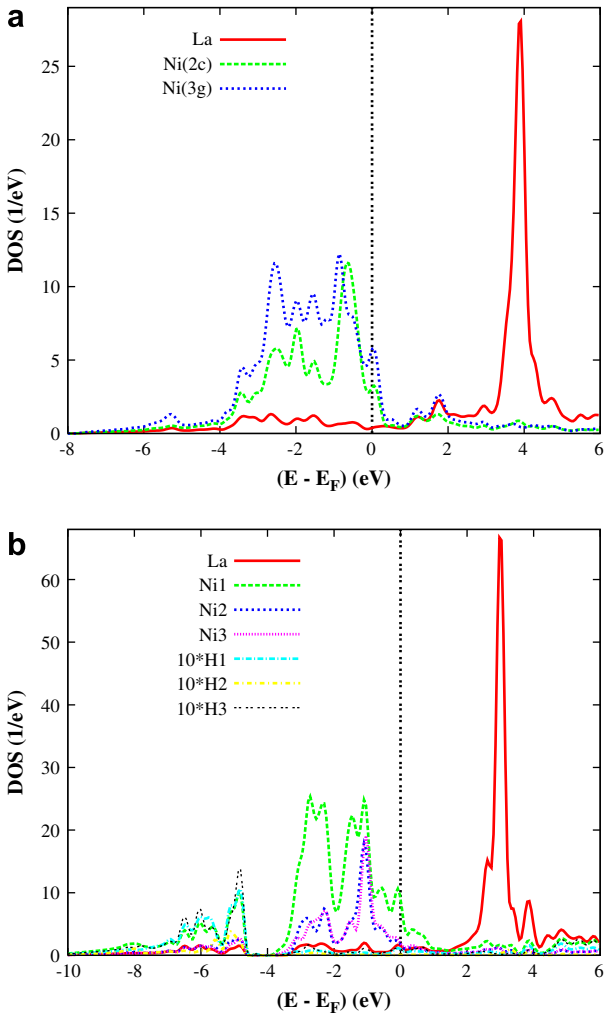

Fig. 3. (Color online) Non-magnetic site projected DOS for: $LaNi_5$ (a) and its $\beta 1$ model for the saturated hydride system (b).

The similar skylines between the partial PDOS pointing to the overlap between Ni and La states can be seen at the lower part of the valence band (VB), with mainly *sp* like states between −6 and −2.5 eV, as well as towards the top of VB between both Ni *d* states. Lastly, within the conduction band (CB), lanthanum *f* states are found dominant which is due to their emptiness.

On the other hand, the characteristic features of the (PDOS) for the saturated hydride system are shown in Fig. 3(b) in which hydrogen PDOSs are artificially magnified by a factor of 10 for a clearer view. A significant enlargement to the extent of 2 eV is noticed for the VB with respect to $LaNi_5$. This is due to the presence of hydrogen *s* states. The energy range from −10 to −4.7 eV comprises hydrogen and lanthanum *s* states as well as nickel *s* and *p* states. The dominant intensity of H1(3) PDOSs with respect to H2 is relevant to the larger site multiplicities of the former two which amount to 6 for both with respect to a multiplicity of 2 for the latter. Another important feature is the dominant Ni1 intensity with respect to all the other atomic constituents which is related to the presence of Ni1 in all three hydrogen insertion sites as shown in Fig. 1(a). This is contrary to Ni2(3) which are found in two and one hydrogen absorption interstices respectively. From this one can expect to have dominant Ni1–H interaction which will be checked in within the chemical bonding section. Further, the similar shapes of the peaks for PDOSs of the different species within this lower part of the VB point to an overlap. Within the itinerant part of the VB, *i.e.* from −4 eV up to E_F, Ni1 3*d* states PDOS are of dominant intensity. Interestingly Ni2(3) 3*d* states show very low PDOSs at E_F which is indicative of a stability of the system in a degenerate spin configuration as far as nickel atoms are responsible of the onset of magnetic moments in case of a magnetic ground state. A quantum mixing is also observed for the PDOSs peak shapes of the latter states throughout the itinerant part of the VB. This peculiar aspect could be related to their similar site multiplicities as well as to their positioning within the octahedral hydrogen absorption hole (see Fig. 1(a)). Lanthanum 4*f* states are found, as expected, above E_F. These states are more localized and intense from their sharper and higher intensity shape as with respect to pure $LaNi_5$.

5.1.2. Analysis of the DOS within stoner theory

The Stoner theory of band ferromagnetism [11] can be applied to address the spin polarization. The total energy of the spin system results from the exchange and kinetic energies counted from a NM state. Formulating the problem at zero temperature, one can express the total energy as

$$E = \frac{1}{2}\left[\frac{m^2}{n(E_F)}\right][1 - In(E_F)].$$

Here *I* is the Stoner exchange integral, which is an atomic quantity that can be derived from spin polarized calculations [45]. $n(E_F)$ is the PDOS value for a given species at the Fermi level in the NM state. The product $In(E_F)$ from the expression above provides a criterion for the stability of the spin system. The change from a NM configuration towards spin polarization is favorable when $In(E_F) \geq 1$. The system then stabilizes through a gain of energy due to exchange. $I(\mathrm{Ni}3d)$ is found to be $\sim$0.5 eV [45]. The computed $n(E_F)$ values of Ni 3*d* states at the 2c and 3g sites for pure $LaNi_5$ are to the extent of 1.55 and 1.86 eV^{-1}. These result into calculated values for $I(\mathrm{Ni}3d)$ of 0.78 and 0.94 for 2c and 3g occupation sites respectively. Then a magnetic instability can be expected for the pure alloy with a possibility of a magnetic moment carried mainly by the nickel atoms lying at the 3g position. This is opposite to the paramagnetic ground state of this system as found by the experiment and will be checked within the SP calculations for further confirmation. On the other hand, the computations performed for

the $\beta 1$ model result into $n(E_F)$ values such as 1.52, 0.59 and 0.71 eV^{-1} for Ni1, Ni2 and Ni3 respectively. Their calculated Stoner products amount to 0.76, 0.29 and 0.36 respectively which indicate that the hydride system ground state is NM.

5.1.3. Bonding characteristics

Chemical bonding properties can be addressed on the basis of the spin degenerate calculations. This is due to the fact that the SP electronic bands, to a large extent, result from the spin degenerate bands by a rigid spin splitting. Fig. 4(a) and (b) shows the ECOV plots respectively with all atoms from metal–metal interactions within $LaNi_5$ and the $\beta 1$ model. A visual inspection of Fig. 4(a) shows that the dominant interaction within the VB occurs between Ni(2c) and Ni(3g). Although this interaction is of a bonding character within the energy interval ranging from −5 to −1.5 eV it shows a larger antibonding behavior from −1.5 eV and up to E_F. These two opposite binding strengths compensate each other. It remains to discuss the interactions of lanthanum states with nickel at 2c and 3g sites respectively which are both bonding within the VB. Such a feature can be commented with respect to the interatomic distances whereas the smaller the distance is the stronger is the interaction. The calculated La–Ni(2c) and La–Ni(3g) separations are to the extent of 2.89 and 3.2 Å respectively. This is significant of a stronger La–Ni(2c) bond with respect to La–Ni(3g) but the larger number of Ni(3g) atoms within the lattice compensates the distance factor and explains the found similarity. Also one can notice the almost null values for both interactions at E_F which point to their contribution to the onset of a magnetic moment if the prediction by the Stoner criterion from the former sections are correct. Turning to the $\beta 1$ model (Fig. 4(b)) a similar conclusion can be drawn around the characters of all Ni–Ni interactions. As for La–Ni1/2/3 interactions respectively, they show bonding characters from −7 to −1.5 eV that change into antibonding from −1.5 eV and up to E_F. La–Ni1 is the strongest in the bonding interval but its higher antibonding intensity rules it out from being responsible for the stability of the system. The latter is relevant to La–Ni2(3) interactions in which La–Ni2 is slightly dominant. This is concomitant with the interatomic distances amounting to 3.07 and 3.09 Å for the La–Ni2 and La–Ni3 separations respectively.

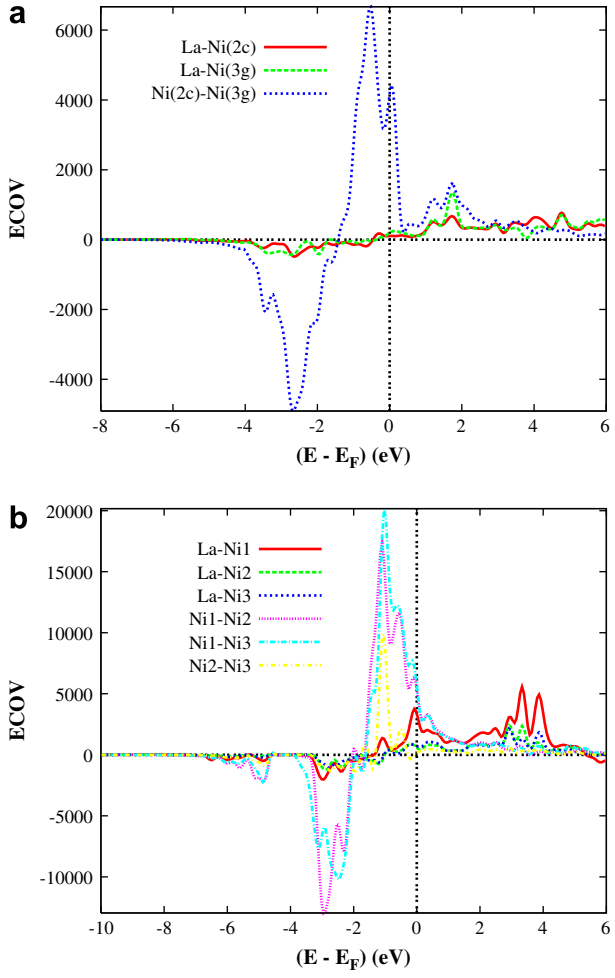

Fig. 4. (Color online) Non-magnetic ECOV plots of lanthanum–nickel interactions for: $LaNi_5$ (a) and its $\beta 1$ model for the saturated hydride system (b).

5.2. Discussion of the magnetic structure

From the non spin polarized (NSP) calculations and their analysis within the Stoner mean field theory of band ferromagnetism, it has been established that $LaNi_5$ is unstable in such a configuration. Consequently, SP calculations were carried out, assuming implicitly a hypothetic ferromagnetic order. This is done by initially allowing for two different spin occupations, then the charges and the magnetic moments are self-consistently converged. The relative energy difference ($\Delta E = E(\mathrm{SP}) - E(\mathrm{NSP})$) for spin degenerate and SP calculations amounts to 0 eV which is a first indication that there is no tendency for spin polarization.

A simple model established by Malik et al. [43] around the magnetic structure of RCo_5 (R = rare-earth) compounds in 1977 predicted that the three valence electrons of the rare-earth metal would fill up the holes in the ↓ -spin Ni 3*d* band. That would reduce the magnetic moment near to zero. Such calculations showed a transfer of only about one rare-earth electron in each case. A larger charge transfer to the extent of 1.5 electrons per lanthanum was noticed by the same authors [7] which resulted into a total moment of $0.69\mu_B$ per formula unit (fu) almost entirely due to nickel as far as there was a zero moment induced at the lanthanum site. Thus the authors referred to $LaNi_5$ as a *"very weak"* ferromagnet with charge transfer and therefore an almost filled ↓ -spin band. Within the current calculations, the VB configuration of the converged SP calculations for various atoms of $LaNi_5$ is as follows:

$$La : 4f_{\uparrow}^{0.24} 4f_{\downarrow}^{0.24} 5d_{\uparrow}^{0.95} 5d_{\downarrow}^{0.95} 6s_{\uparrow}^{0.27} 6s_{\uparrow}^{0.27}$$
$$Ni(2c) : 3d_{\uparrow}^{4.27} 3d_{\downarrow}^{4.27} 4s_{\uparrow}^{0.32} 4s_{\uparrow}^{0.32}$$
$$Ni(3g) : 3d_{\uparrow}^{4.25} 3d_{\downarrow}^{4.25} 4s_{\uparrow}^{0.34} 4s_{\uparrow}^{0.34}$$

It is clear from the outer electron configurations that the 6*s* bands of lanthanum as well as 4*s* nickel bands give away charges to the extent of ∼1.5 and ∼1.3 respectively. These are distributed among the other bands resulting into an equally filled ↑ and ↓ subbands. Further a small *f* character for La and a larger filling of La and Ni *d* states are noticed. So one can talk about a charge transfer between the different species which is depicted by the ELF mapping of Fig. 1(b) showing distorted pentagons. The equal occupation of subbands leads to a null total magnetic moment. This feature along with the instability of the NM configuration (Stoner criterion) is indicative of a paramagnetic ground state which agrees with the experiment.

Another significant parameter can be extracted from the calculations and compared with the experiment namely the electronic specific-heat coefficient γ which is given by the following formula: $\gamma = (2/3(\pi^2 k_B^2)) \times N(E_F)$. The computed value of γ for $LaNi_5$ is evaluated to be 23.12 $mJ \times K^{-2} \times mol^{-1}$. This is to be compared with the experimental values of 34.3 and 36.5 $mJ \times K^{-2} \times mol^{-1}$ [46,47]. The discrepancy from the

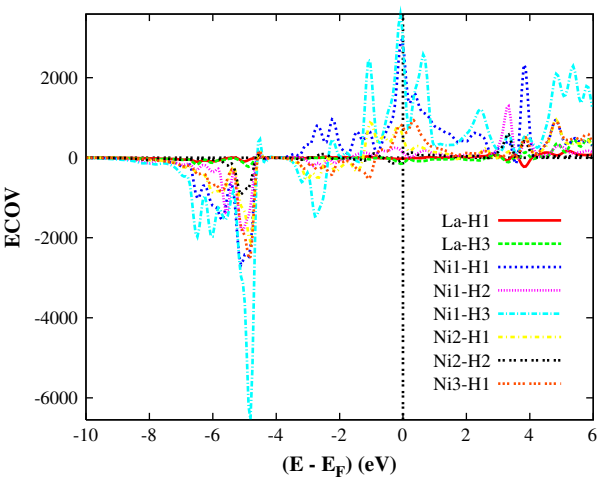

Fig. 5. (Color online) Non-magnetic ECOV plots of the hydrogen–other atomic constituent's interactions for the $\beta 1$ model for the saturated hydride system.

experiment is ascribed to electron–phonon enhancement effects encountered by the experiment. Previous APW calculations [7] came with a good agreement to the experiment with a γ value to the extent of 32.4 mJ $\times$ K^{-2} $\times$ mol^{-1}. More recent LMTO-ASA and FP-LMTO computations [8] obtained values such as 22.8 and 22.4 mJ $\times$ K^{-2} $\times$ mol^{-1}.

Neither experimental works nor the Stoner criterion for band ferromagnetism applied here pointed to a magnetic behavior of the saturated hydride system. Also SP calculations resulted into a null total magnetic moment. A need to check the magnetovolume effects relevant to volume expansion was answered by calculating two models at the saturated hydride volume and the SGs of both $\beta 1$ model and $LaNi_5$ respectively. The second calculation was achieved by considering a large supercell along the *c*-axis in order to reduce any overlapping problems encountered with the expansion of a simple cell as far as the saturated hydride is described by a double cell (see Section 2). Both models converged to a large total magnetic moment amounting to $\sim 3\mu_B$. To explain the absence of such large magnetization within the hydride, the bonding between hydrogen and the different species is plotted in Fig. 5. An analysis of the plotted curves shows that the dominant interactions are of bonding character and they lye in the energy region ranging from -8 to -4 eV. The most important interactions are seen between Ni1 and hydrogen which are relevant to the presence of Ni1 as a constituent of all H insertion holes, especially the tetrahedral site with H in the 6c position whereby Ni–H3 is the most bonding interaction. This meets with the ELF mapping in Fig. 1(a) where a strong localization is seen around H3.

6. Conclusion

In this work hydrogen storage material $LaNi_5$ and its saturated hydride have been theoretically investigated within DFT. Hypothetic intermediate hydride models with SGs of both the pure alloy [$LaNi_5H_3(Z=1)$, $La_2Ni_{10}H_6(Z=2)$] and the saturated hydride [$La_2Ni_{10}H_6(Z=1)$] were also computed. Pending questions have been answered, relevant to (i) the SG of the saturated hydride as far as previous experimental works as well as theoretical computations could not rule out either two suggested symmetries, *i.e. P6$_3$mc* and *P31c*, (ii) the ground state of $LaNi_5$ which was defined as paramagnetic by the experiment and ferromagnetic by theoretical computations and (iii) the interplay between the magnetovolume effects and the bonding of hydrogen in the host lattice. PP calculations gave $E(V)$ curves from which equilibrium quantities such as energies, volumes and bulk modulus were extracted. From the energy values it was shown that hydrogen is more bound in the lattice of the saturated hydride with respect to the intermediate hydride models. Further the hydrogen is more bound in a double cell such as $La_2Ni_{10}H_6$ ($Z=1$) with respect to $LaNi_5H_3$ ($Z=1$) and $La_2Ni_{10}H_6$ ($Z=2$). This provides an explanation of the cell doubling upon H uptake. Both saturated hydride models were examined resulting into a small total energy difference of 0.015 eV which is not sufficient to discard either of the two SGs. The PP calculations were also used for geometry optimizations of the different models from which the input parameters to all-electrons ASW calculations were generated. ASW computations defined, from the saturated hydride models energy difference of 1.65 eV, *P6$_3$mc* as the most plausible SG. The use of the GGA approximation parameterized by Wu and Cohen resulted into a NM configuration pointing to a magnetic instability on the nickel 3g site. Subsequent SP computations converged into a null value for the total magnetic moment. These two features point that the ground state configuration for this pure alloy is between NM and ferromagnetic which is the paramagnetic order concomitant with the experiment. Although volume expansion introduced by hydrogenation implies the onset of a total magnetic moment, the hydrogen binds with the different constituents, namely with nickel, to block this magnetization. This results into a NM saturated hydride system.

Acknowledgments

Computational facilities were provided by the M3PEC-Mésocentre of the University Bordeaux 1, financed by the "Conseil Régional d'Aquitaine" and the French Ministry of Research and Technology. One of us S.F.M. acknowledges financing by the French Embassy in Beirut, SCAC services, for on site missions at USEK.

References

[1] J.H.N. Van Vucht, F.A. Kuijpers, H.C.A.M. Bruning, Philips Res. Rep. 25 (1970) 133.
[2] F. Cuevas, J.-M. Joubert, M. Latroche, A. Percheron-Guégan, Appl. Phys. A 72 (2001) 225.
[3] W.E. Wallace, R.F. Karllcek Jr., H. Imamura, J. Phys. Chem. 83 (1979) 1708.
[4] P. Fisher, A. Furrer, G. Busch, L. Schlapbach, Helv. Phys. Acta 50 (1977) 421.
[5] C. Lartigue, A. Le Bail, A. Percheron-Guégan, J. Less-Common Met. 129 (1987) 65.
[6] W.E. Wallace, Rare Earth Intermetallic, Academic, New York, 1973, pp. 129.
[7] S.K. Malik, F.J. Arlinghaus, W.E. Wallace, Phys. Rev. B 25 (1982) 6488.
[8] I. Tadaei, I. Hideaki, J. Appl. Phys. 97 (2005) 10A313.
[9] P. Hohenberg, W. Kohn, Phys. Rev. B 136 (1964) 864.
[10] W. Kohn, L.J. Sham, Phys. Rev. A 140 (1965) 1133.
[11] J. Kübler, V. Eyert, Electronic Structure Calculations, in: K.H.J. Buschow (Ed.), Materials Science and Technology, Electronic and Magnetic Properties of Metals and Ceramics, Part I. Volume, vol. 3A, VCH, Verlag, Weinheim, 1992, pp. 1–145.
[12] R. Hempelmann, D. Richter, G. Eckold, J. Less-Common Met. 104 (1984) 1.
[13] J.L. Sobeyroux, A. Percheron-Guegan, J.C. Achard, J. Less-Common Met. 129 (1987) 181.
[14] E.H. Kisi, E.M.A. Gray, S.J. Kennedy, J. Alloys Comp. 216 (1994) 213.
[15] D.G. Westlake, J. Less-Common Met. 91 (1983) 275.
[16] G. Kresse, J. Furthmüller, Phys. Rev. B 54 (1996) 11169.
[17] P.E. Blöchl, Phys. Rev. B 50 (1994) 17953.
[18] G. Kresse, J. Joubert, Phys. Rev. B 59 (1999) 1758.
[20] J. Perdew, K. Burke, M. Ernzerhof, Phys. Rev. Lett. 77 (1996) 3865.
[21] M. Methfessel, A.T. Paxton, Phys. Rev. B 40 (1989) 3616.
[22] H.J. Monkhorst, J.D. Pack, Phys. Rev. B 13 (1976) 5188.
[23] A.D. Becke, K.E. Edgecombe, J. Chem. Phys. 92 (1990) 5397.
[24] A.D. Becke, K.E. Edgecombe, Nature 371 (1994) 683.
[25] A.R. Williams, J. Kübler, C.D. Gelatt, Phys. Rev. B 19 (1979) 6094.
[26] V. Eyert, The Augmented Spherical Wave Method – A Comprehensive Treatment, , In: Lect. Notes Phys, vol. 719, Springer, Berlin Heidelberg, 2007.
[27] Z. Wu, R.E. Cohen, Phys. Rev. B 73 (2006) 235116.
[28] V. Eyert, K.-H. Höck, Phys. Rev. B 57 (1998) 12727.
[29] V. Eyert, J. Comput. Phys. 124 (1996) 271.
[30] A.F. Al Alam, S.F. Matar, N. Ouaïni, M. Nakhl, Prog. Solid State Chem. 36 (2008) 192.

[31] S.F. Matar, J.F. Riecken, B. Chevalier, R. Pöttgen, A.F. Al Alam, V. Eyert, Phys. Rev. B 76 (2007) 174434.
[32] A.F. Al Alam, S.F. Matar, N. Ouaïni, M. Nakhl, Eur. Phys. J. B 65 (2008) 491.
[33] R. Hoffmann, Angew. Chem. Int. Ed. Engl. 26 (1987) 846.
[34] R. Dronskowski, P.E. Blöchl, J. Phys. Chem. 97 (1993) 8617.
[35] G. Bester, M. Fähnle, J. Phys: Condens. Matter 13 (2001) 11541.
[36] K. Tatsumi, I. Tanaka, H. Inui, K. Tanaka, M. Yamaguchi, H. Adachi, Phys. Rev. B 64 (2001) 184105.
[37] P.W. Atkins, Molecular Quantum Mechanics, second ed. Oxford University Press, Oxford, 1983, p. 257.
[38] J.J. Murray, M.L. Post, J.B. Taylor, J. Less-common Met 80 (1981) 211.
[39] W.N. Hubbard, P.L. Rawlins, P.A. Connick, R.E. Stedwell Jr., P.A.G. O'hare, J. Chem. Thermodyn. 15 (1983) 785.
[40] D. Chen, G.-L. Xu, X.-W. Zhang, Y.-L. Zhao, B.-H. Yu, H. D-Shi, Chin. Phys. Lett. 25 (2008) 2950.
[41] K. Tanaka, S. Okazaki, T. Ichitsubo, T. Yamamoto, H. Inui, M. Yamguchi, M. Koiwa, Intermetallics 8 (2000) 613.
[42] S.F. Matar, Prog. Solid State Chem. 31 (2003) 239.
[43] S.K. Malik, F.J. Arlinghaus, W.E. Wallace, Phys. Rev. B 16 (1977) 1242.
[44] H. Nakamura, D. Nguyen-Manh, D.G. Pettifor, J. Alloys Comp 281 (1998) 81.
[45] J.F. Janak, Phys. Rev. B 16 (1977) 255.
[46] S. Nasu, H.H. Neumann, N. Marzouk, R.S. Craig, W.E. Wallace, J. Phys. Chem. Solids 32 (1971) 2779.
[47] T. Takeshita, G. Dublon, O.D. McMasters, K.A. Gschneidner Jr., in: G.J. McCarthy, J.J. Rhyne, H.B. Silber (Eds.), The Rare Earths in Modern Science and Technology, Plenum, New York, 1980, p. 563.